



Mineral dissolution by dimeric complexes

Xiaoxu Li^{a,1}, Qing Guo^{b,1}, Yatong Zhao^{a,c,1}, Chang Qian^d, Maxime Pouvreau^a, Trent R. Graham^a, Ping Chen^a, Lili Liu^a, Chang Liu^d, Benjamin A. Legg^a, Qian Chen^d, Aijun Miao^c, Zheming Wang^a, James J. De Yoreo^{a,e}, Carolyn I. Pearce^f, Aurora E. Clark^{a,b,2}, Kevin M. Rosso^{a,2}, and Xin Zhang^{a,2}

Edited by Risto Nieminen, Aalto-yliopisto Teknillisen fysiikan laitos, Espoo, Finland; received February 24, 2025; accepted August 14, 2025

Mineral dissolution is typically thought to occur by the detachment of monomeric building blocks of the crystal structure, although direct evidence is rare. Using in situ high-speed atomic force microscopy to examine step-edge retreat dynamics at high resolution, we report that the dissolution of gibbsite in alkaline solutions occurs mainly by the release of aluminate dimers, which subsequently dissociate into the monomeric species that dominate the solution. The observed dissolution anisotropy is readily explained by this mechanism, which was further supported by density functional tight-binding simulations of detachment activation energies. Recognition that such polynuclear dissolution mechanisms exist may enable an improved understanding of processes regulating mineral dissolution rates in nature and industry.

mineral dissolution | atomic force microscopy | density functional tight-binding simulations | machine learning

Mineral dissolution is a fundamental interfacial process with broad relevance across materials science, earth sciences, and pharmaceutics (1). An in-depth understanding of dissolution mechanisms is crucial for precision control in micro- and nanoscale etching, the development of predictive models for weathering and carbon mineralization, and the management of radioactive waste (2). Viewed through the lens of the terrace-ledge-kink (TLK) framework, this understanding requires insight at the molecular scale into reactive site structure (e.g., kink sites) (3) as well as the mechanism governing the detachment and propagation of these sites (4, 5). Most dissolution models assume a monomer-bymonomer detachment mechanism (5), where "monomers" include individual ions, ion pairs, or monomeric aqua complexes. Despite advances in atomically resolved imaging that now allow for routine characterization of kink site propagation (6, 7), direct evidence of the detaching group of dissolution remains limited. This lack of direct evidence complicates mechanistic interpretations, particularly for anisotropic dissolution patterns observed at step edges. Accurately characterizing these anisotropic patterns requires rationalizing the reactivity of specific surface-bound monomers, considering local structural interactions that extend beyond first-order neighbors (8-10), which implies the dynamics of dissolution are constrained by the structure of multi-ion clusters rather than monomers.

An alternative hypothesis, often overlooked, is the prospect that the detaching group may exceed monomer size. Gibbsite (γ-Al(OH)₃) dissolution in alkaline solutions provides a case in point. In alkaline solutions, the equilibrium that defines gibbsite solubility is simply $Al(OH)_3$ (s) + $OH^- = Al(OH)_4^-$ (aq), which entails a coordination change of Al from octahedral in gibbsite to tetrahedral in the solubilized oxyanion (11–14). Despite its apparent simplicity and relevance to alumina refining, nuclear waste management (15), and Al-mobility in natural hyperalkaline environments (16), the underlying mechanism of this transformation has been elusive. Macroscopic dissolution kinetics reported that the dissolution rate depended on the concentration of Al^{III} in the solution to the powder of two, hinting at a possible dimer-based dissolution mechanism (17), but direct evidence

The present study examines the dissolution of gibbsite in alkaline solutions, seeking to isolate the molecular identity of the detaching group. The advent of high-speed atomic force microscopy (HS-AFM) provides an opportunity to directly observe the dissolution process at near-atomic resolution and timescales consistent with detachment events. Through the integration of HS-AFM, machine-learning-assisted surface structure reconstruction, bulk dissolution kinetics, and molecular dynamics simulations, we identify the reactive sites involved in gibbsite dissolution in alkaline solutions. Our findings provide clear evidence for a dimeric detaching group, offering a more straightforward explanation for the observed dissolution morphology compared to the traditional monomeric dissolution model. These insights into dissolution take on added importance in understanding the mechanisms of crystallization (4, 18, 19). In the last couple of decades, nonclassical

Significance

Mineral dissolution is central to weathering, reactive flow and transport, ore processing, and more. Interpreting observed rates in terms of a molecular scale dissolution mechanism often requires assumptions about the detaching group. The finding that monomeric building blocks can detach more readily as pairs forces us to rethink those assumptions and refine mechanistic models to more reliably predict dissolution rates across a range of conditions.

Author affiliations: ^aPhysical & Computational Science Directorate, Pacific Northwest National Laboratory, Richland, WA 99354; bDepartment of Chemistry, The University of Utah, Salt Lake City, UT 84112; cState Key Laboratory of Pollution Control and Resource Reuse, School of the Environment, Nanjing University, Nanjing, Jiangsu Province 210023, China; ^dDepartment of Materials Science and Engineering, Materials Research Laboratory, Beckman Institute for Advanced Science and Technology, University of Illinois at Urbana-Champaign, Urbana, IL 61801; eDepartment of Materials Science and Engineering, University of Washington, Seattle, WA 98195; and ^fEnergy and Environment Directorate, Pacific Northwest National Laboratory, Richland, WA 99354

Author contributions: X.L., A.E.C., K.M.R., and X.Z. designed research; X.L., Q.G., Y.Z., C.Q., M.P., T.R.G., P.C., L.L., and X.Z. performed research; X.L., Q.G., Y.Z., C.Q., M.P., T.R.G., L.L., Q.C., Z.W., C.I.P., A.E.C., K.M.R., and X.Z. contributed new reagents/analytic tools; Q.G., Y.Z., C.Q., M.P., T.R.G., C.L., B.A.L., A.M., J.J.D.Y., K.M.R., and X.Z. analyzed data; B.A.L., Q.C., A.M., Z.W., J.J.D.Y., C.I.P., and A.E.C. discussion and manuscript revision; and X.L., Q.G., K.M.R., and X.Z. wrote the paper.

The authors declare no competing interest.

This article is a PNAS Direct Submission.

Copyright © 2025 the Author(s). Published by PNAS. This article is distributed under Creative Commons Attribution-NonCommercial-NoDerivatives License 4.0

¹X.L., Q.G., and Y.Z. contributed equally to this work.

²To whom correspondence may be addressed. Email: aurora.clark@utah.edu, kevin.rosso@pnnl.gov, or xin. zhang@pnnl.gov.

This article contains supporting information online at https://www.pnas.org/lookup/suppl/doi:10.1073/pnas. 2504109122/-/DCSupplemental.

Published October 6, 2025.

hierarchical crystallization pathways via attachment of dimers (20–24), oligomers (25, 26), and particles (27, 28), instead of a monomer-by-monomer attachment, have been widely reported (28–31). The findings reported here extend recent studies demonstrating dissolution by particle detachment (32) to yet another hierarchical pathway and help reconcile the complex picture of nonclassical crystal growth with what has, to date, been a much simpler picture of dissolution.

Results and Discussion

Crystallographic Control of Gibbsite Anisotropic Dissolution. Wellcrystalline pseudohexagonal gibbsite nanoplates were synthesized using methods previously reported (33, 34), as confirmed by transmission electron microscopy (TEM) (Fig. 1A and SI Appendix, Fig. S1) and X-ray diffraction (XRD) (SI Appendix, Fig. S2). The crystallographic orientation of these plates was determined from TEM selective area electron diffraction (Fig. 1A; for more details, see SI Appendix, Supplementary Text). Gibbsite is known for its layered structure, where a single layer comprises hexacoordinated Al³⁺ cations occupying two-thirds of the octahedral interstices between close-packed OH planes. This arrangement forms the well-known honeycomb dioctahedral sheet, a major building block for phyllosilicates. It exhibits a nominal trigonal symmetry (Fig. 1B) (35). These Al(OH)₃ layers are interconnected along the stacking direction by hydrogen bonds and follow an AB-BA stacking sequence (Fig. 1D). AFM images routinely revealed the presence

of two growth spirals on the gibbsite (001) basal plane (Fig. 1C). These spirals emanate from a central double screw dislocation, with a Burgers vector equal to one unit cell (Fig. 1E). Similar screw dislocations have been documented in natural gibbsite crystals (36) and Bayer-process gibbsite (37), indicating that such defects are ubiquitous in both geological and industrial settings. There are two general types of step edge terminations observed for each gibbsite layer (38): the "zigzag" type (consisting of the six equivalent edges oriented perpendicular to the [1 0 0], [1 1 0], and [1 1 0] directions or their inverses), and the "armchair" type (consisting of the six edges oriented perpendicular to the [130], [0 1 0], and [1 $\overline{3}$ 0] directions or their inverses) (Fig. 1F). The armchair terminations are further divided into acute and obtuse types. This classification depends on whether the outermost hydroxyl of the terminating octahedra points toward or away from the surface (Fig. 1 D and F). According to TEM and AFM images, gibbsite nanoplates have zigzag terminations comprising the edge faces of the nanoplates.

We used in situ AFM to monitor gibbsite nanoplates dissolving in NaOH solution at room temperature (Movie S1). After introducing NaOH, the step edges of two spirals continuously retreated inward, reducing the height of the basal plane (Fig. 2A). The step heights associated with each spiral (0.5 nm) correspond to a single layer of gibbsite (Fig. 2B). The patterns of dissolution remained the same over the range of NaOH concentrations tested (0.01 M to 0.4 M), and we did not observe any opening of etch pits at the dislocation or elsewhere on the crystal face (SI Appendix, Figs. S3–S6).

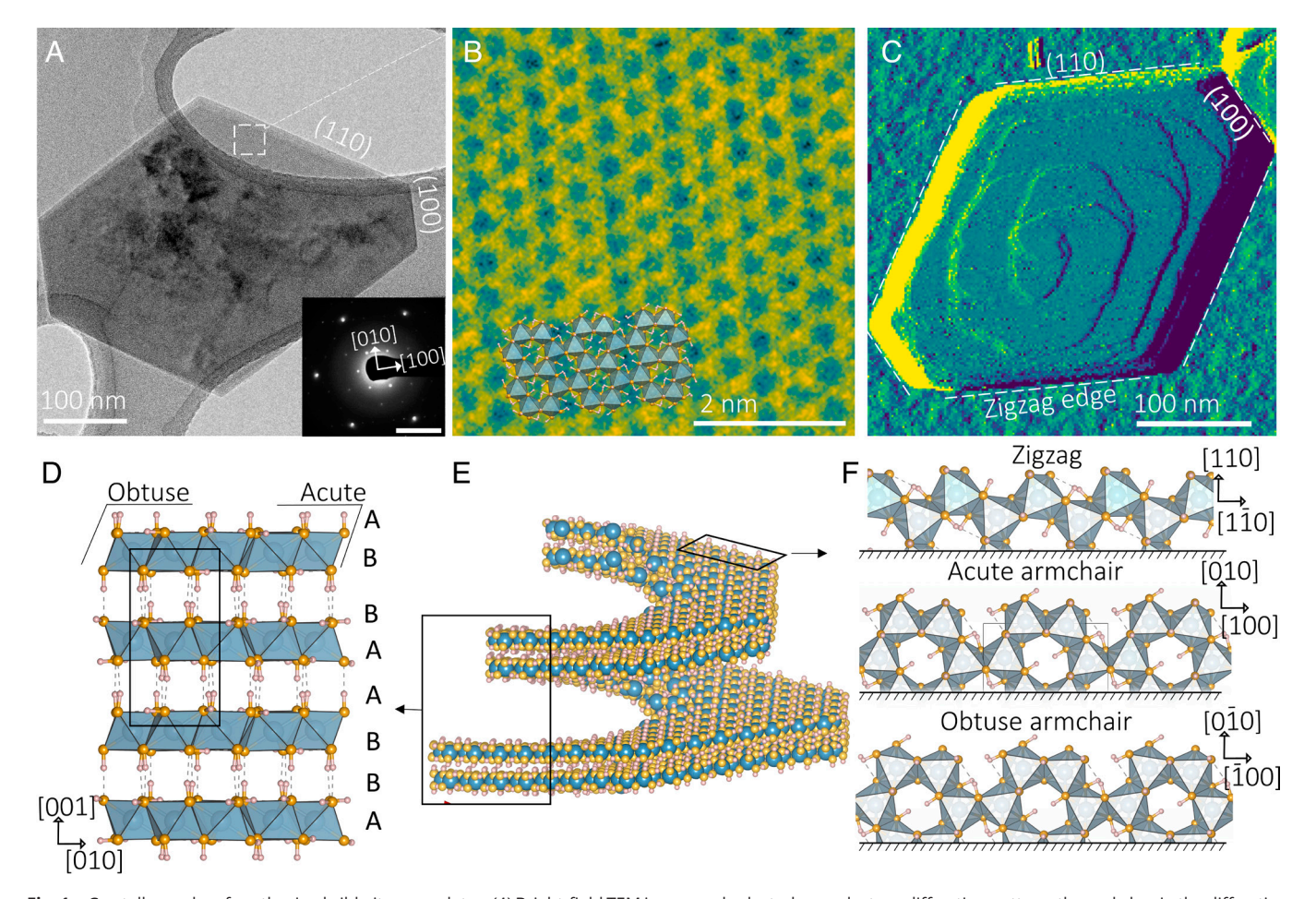


Fig. 1. Crystallography of synthesized gibbsite nanoplates. (*A*) Bright-field TEM image and selected area electron diffraction pattern; the scale bar in the diffraction pattern is 5 nm $^{-1}$. (*B*) High-resolution TEM image of gibbsite basal plane shows the honeycomb pattern of the dioctahedral sheet. (*C*) AFM phase image of gibbsite nanoplates on the TiO $_2$ (001) wafer. (*D*) Crystal structure of gibbsite sheets; the black box indicates the unit cell. (*E*) Sketch of screw dislocation of gibbsite with Burger's vector equal to one unit cell. (*F*) Structures of gibbsite terminations: zigzag edge, acute armchair edge, and obtuse armchair edge.

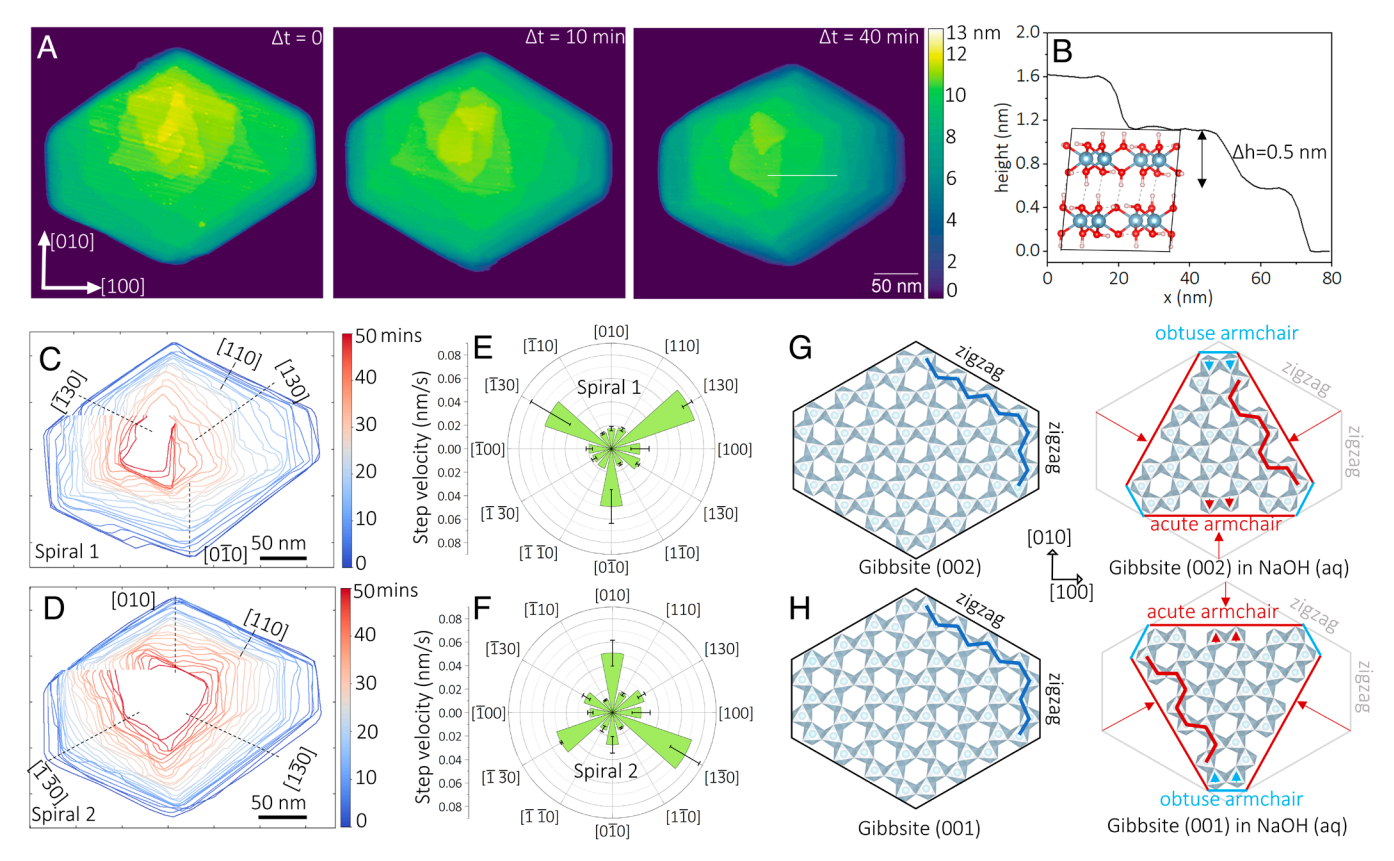


Fig. 2. Crystallographic control of gibbsite anisotropic dissolution in NaOH. (4) AFM height images of a single gibbsite nanoplate dissolving in 0.05 M NaOH solution on TiO₂ (001) wafer. (B) Height profile of the gibbsite basal surface. (C and D) Contour plots of spiral 1 and 2 within one single period. (E and F) Apparent direction-specific velocities of the step edges of spiral 1 and 2 as functions of step edge orientation. The average values and SD of velocities were measured from more than 10 edges for each direction. (G and H) Sketches of the adjacent gibbsite single sheets (002) and (001), showing the structural transformation of the edge from a zigzag type to an acute armchair type due to the preferential dissolution of the acute armchair. Hydrogen and oxygen atoms are hidden for clarity. Red and blue arrows distinguish acute and obtuse armchairs, respectively.

To better elucidate the reactive sites and dissolution kinematics, we constructed contour plots of two spirals as a function of dissolution time in various NaOH solutions (0.05 M) (Movie S2). These plots (Fig. 2 C and D) show the step edge evolution within one single period and the apparent average retreat velocities (Fig. 2 E and F) of two spirals as a function of orientation. The data show that dissolution begins at the corners of two zigzag edges of each layer. As this process progresses, straight armchair edges develop due to their higher velocities, which gradually consume the zigzag edges. Specifically, for spiral 1, the step edges in [1 3 0], [0 1 0], and $[\overline{1} \ 3 \ 0]$ directions dissolve preferentially (Fig. 2E), causing the spiral to retreat inward and form an equilateral triangle spiral (Fig. 2C). In contrast, spiral 2 evolves similarly but with the reverse directional preference, namely [13 0], [0 1 0], and [1 3 0] (Fig. 2 D and F). We note that these dissolving step edges all have the same armchair-type morphology (see sketch in Fig. 2 *G* and *H*). Previous AFM observations (36) and molecular simulations (39) show that the zigzag edges are more stable against proton or hydroxyl attack than armchair-type step edges on the gibbsite basal plane. However, our analysis presents a different perspective: within a single layer, one-half of the armchair-type step edges dissolve preferentially. Meanwhile, the apparent retreat velocities of the opposite step edges are as slow as those of the zigzag edges (Fig. 2 E and F). This same pattern of dissolution was observed across a range of NaOH concentrations, from 0.01 to 0.2 M (SI Appendix, Figs. S4–S6).

Our results shed light on the role of crystal symmetry in dictating the complex kinematics of gibbsite dissolution. The anisotropic

nature of this dissolution reflects the trigonal symmetry found in the sheet structure of gibbsite. Specifically, the AB-BA stacking configuration results in mirror-symmetric surface structures between adjacent (0 0 1) and (0 0 2) layers along the crystallographic a-c plane (SI Appendix, Fig. S7). Consequently, the anisotropic dissolution patterns observed in the adjacent spirals (Fig. 2 E and F) exhibit this same mirror symmetry. However, explaining the anisotropic dissolution solely based on the crystal structure proves challenging, especially when considering it in traditional terms of a monomer-by-monomer detachment mechanism. This challenge arises because, in both zigzag and armchair edges, the Al octahedra are linked to the crystal through two edge-sharing Al-(OH)2-Al linkages. These linkages possess equivalent geometrical structures, which, according to the TSK framework, should result in similar stability and dissolution rates. A more contextual understanding emerges when we consider the aluminate dimer (Al-dimer) as the fundamental reactive unit. Indeed, the dimer-like structure has been viewed as the fundamental reactive unit in the ligand exchange of MAl₁₃ Keggin (40). As indicated in Fig. 1F, Al-dimers in zigzag edges have three Al-(OH)₂-Al linkages to the crystal, whereas, in armchair edges, Al-dimers are connected by only two Al-(OH)2-Al linkages, corresponding to the observed stability of zigzag edges. Since the connections of armchair dimers and monomers with the crystal are the same, the detachment of dimers from armchair edges is likely more efficient. Crucially, the Al-dimers in opposing armchair edges are not equivalent in their linkages with the crystal. This difference results in the formation of obtuse- and acute-angled armchair edges (Fig. 1 D and F). The kinematic features from AFM studies align with this understanding. The observed patterns in AFM can be replicated if one type of armchair edge is kinetically more favorable for detachment (Fig. 2 *G* and *H*).

Dimeric Aluminate as a Reactive Unit for Dissolution. To further investigate the role of dimeric aluminate in gibbsite dissolution, we employed high-resolution HS-AFM to closely observe the retreat of step edges on the gibbsite basal plane in a 0.1 M NaOH solution (Fig. 3A). We observed that the step edge comprises long [1 1 0] zigzag segments and shorter [1 3 0] armchair segments. This composition was determined by examining the periodic patterns on the terrace. Notably, the length of these armchair edges corresponds to approximately 2 to 3 Al-dimers (Fig. 3B). During the dissolution process, we noted that dissolution commenced from the lower left armchair edges. It then propagated parallel to the [1 1 0] direction, leaving the right zigzag edge—both preexisting and newly formed—unreacted. This microscopic view of dissolution kinematics indicates that the apparent retreat of zigzag edges at the particle level is facilitated by the detachment and subsequent propagation of Al-dimers (Fig. 3B). Consequently, by considering the Al-dimer as the primary reactive kink site, we find a simpler and more elegant explanation for the observed complex dissolution behavior. Conceptually consistent with a TLK picture, the detachment of Al-dimers at these kink sites creates new kinks along the zigzag edge. This process is self-propagating, continuously driving the dissolution forward.

Under different NaOH concentrations, the velocities of reactive armchair edges exhibit a power law dependence on the activity of OH^- with an exponent of 1.50 ± 0.07 (*SI Appendix*, Fig. S8). A reaction order greater than one suggests that the dissolution of the two Al ions in the dimer is interdependent (5, 41). Using a combination of liquid state 27 Al NMR (*SI Appendix*, Fig. S9) and Raman spectroscopy (*SI Appendix*, Figs. S10 and S11), we monitored gibbsite dissolution in 0.2 M NaOH without the formation of new solid phases (e.g., boehmite and other aluminum hydroxide polymorphs) in which the dissolution kinetics followed pseudo-second-order rate

dependence on the concentration of Al(OH)₄ as reported previously (SI Appendix, Supplementary Text) (17, 42). This second-order dependence provides macroscopic evidence for a growth and dissolution mechanism based on the attachment and detachment of dimeric aluminate, as opposed to monomeric aluminate. Mechanistically, this could arise from two scenarios. The dimer (Al₂(OH)₈²⁻) detaches as one unit into the solution through two consecutive OH attacks, followed by dissociation into two soluble $Al(OH)_4^-$ monomers in the bulk solution when [Al] is less than 0.5 M (43). The second step is kinetically favorable due to the low activation energy (2 kcal/mol) required (44). Alternatively, one monomer (Al(OH)₄⁻) in the dimer can begin to detach first, leaving the remaining monomer with only two Al-O-Al bonds connected to the crystal, resulting in a faster dissolution rate so that they are effectively removed as a pair. This would comprise an example of A-B type crystal dissolution, where the distinction between A and B is due to the difference in lattice site, rather than the difference in atom type.

Utilizing atomic-resolution HS-AFM, we capture metastable intermediate states during the dissolution process. As shown in Fig. 4A, the formation of an etch pit on a terrace is observed in a 0.01 M NaOH solution. Due to the high curvature of the small etch pit, the dissolution rate is slow enough to observe the dynamic process of clusters during dissolution, compared to the straight edges. Initially, the surface is a defect-free gibbsite basal terrace. After the first 200 s, we observe the nucleation of an etch pit. The lattice fringes are distorted around the step edges. By $\Delta t = 210$ s, ion clusters begin to form adatoms at the [0 1 0] step edge (indicated as an arrow), likely through the flipping of partially disconnected clusters. The attached ion cluster diffuses along the [0 1 0] direction, as observed at $\Delta t = 215$ s, before detaching at $\Delta t = 240$ s.

To reveal the atomic-level dynamics of intermediate clusters, reconstructing the atomic surface structure from AFM images is essential. However, the convolution of the AFM tip into the AFM data and the surface structure's complexity make precise reconstruction challenging. To address this uncertainty, we employed a

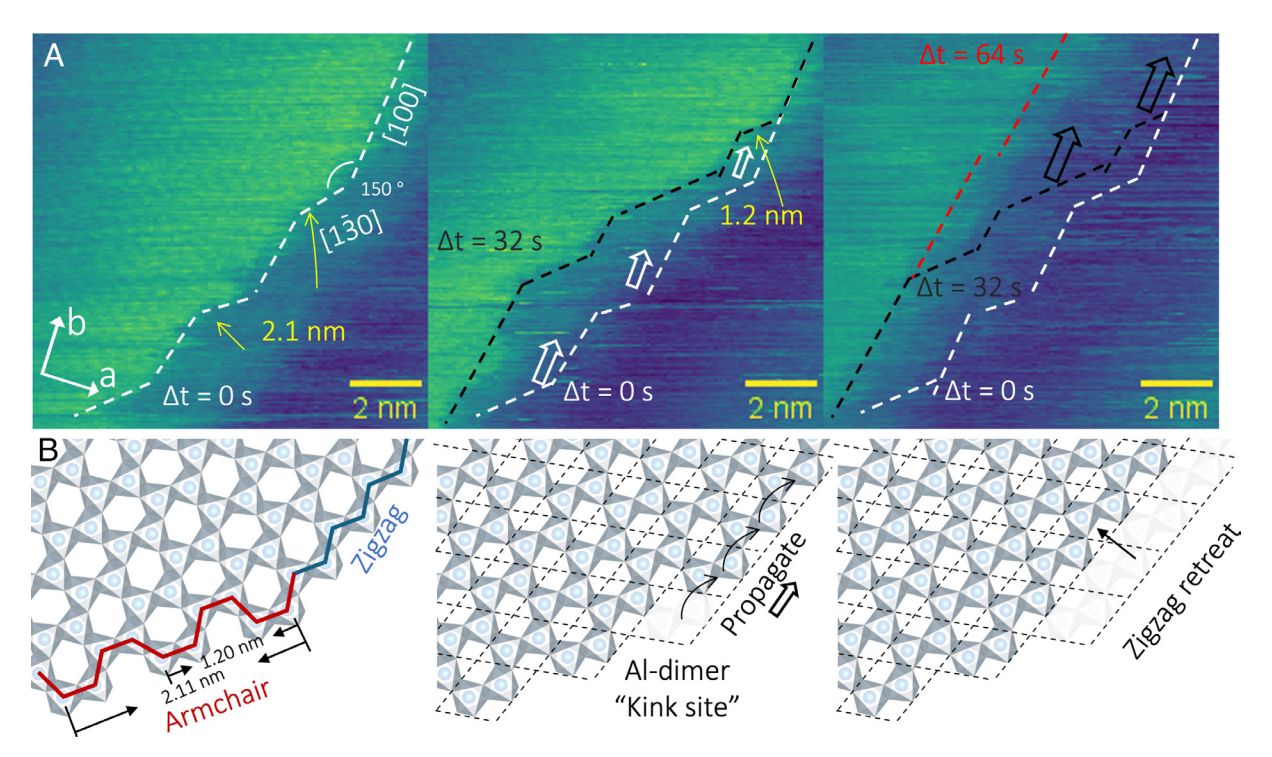


Fig. 3. High-resolution AFM reveals atomic-scale features of step edge retreat. (*A*) Retreat of the step edges on the gibbsite basal plane in a 0.1 M NaOH solution. (*B*) A sketch illustrating how the dimeric aluminum self-generates through dissolution and propagates along the zigzag-type edge.

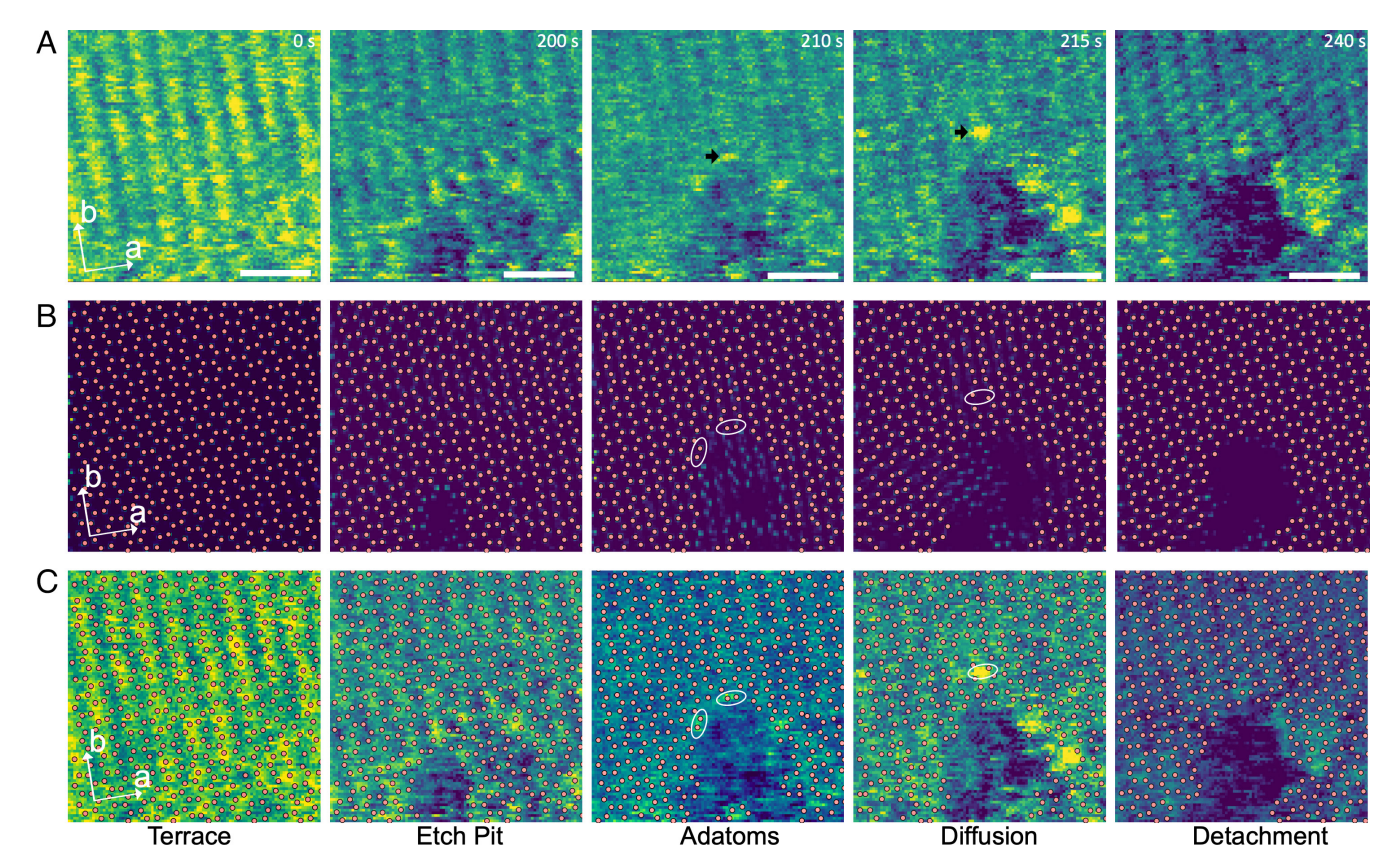


Fig. 4. High-resolution high-speed AFM and machine learning reveal metastable clusters during etch pit formation. The height AFM images of opening etch pit (A), U-net prediction overlaid tracked Al position (B), and the AFM data overlaid with tracked Al position (C). The adatoms are indicated by arrows in AFM images and by cycles in the image of tracked Al positions. The scale bar is 2 nm.

machine learning (ML)-assisted method to reconstruct the surface structure using a simulated AFM images dataset that accounts for the interaction between Si tips and the gibbsite surface (see SI Appendix, Supplementary Text for details). The CLAYFF force field (45) was used to calculate the force-distance (F-z) curve as the sum of the interaction forces between the tip atoms and gibbsite surface atoms (SI Appendix, Fig. S12), considering only the z-direction component of the force. The simulated noise-free AFM images were generated based on the zero-force point of the F-z curve for each pixel, maintaining the same spatial resolution as the experimental images. We also modeled the noise-forming mechanisms in AFM to make the simulated images more comparable to real data by applying a sequence of Gaussian noise, anisotropic offsets, Gaussian blur, additional Gaussian noise, and random bright/dark oval patches (as specified in SI Appendix, Fig. S13). The architecture of the U-Net used in this work is shown in SI Appendix, Fig. S14, and the model training was carried out using TensorFlow and Keras. After U-Net prediction, the model outputs the Al positions as a probability map, from which positions are extracted by identifying local maxima and applying a threshold of 0.15 to filter out prediction noise. Examples of the model's performance on the validation set and real data (SI Appendix, Fig. S15) demonstrate that the ML model can accurately reconstruct the positions of Al atoms on terraces, step edges, and even adatoms.

The tracked Al positions during etch pit formation, along with those overlaid with AFM data, are shown in Fig. 4 B and C, respectively. As indicated by the white circle, the adatoms occupy the Al-dimer positions along the armchair edge, supporting the conclusion that Al dimers can indeed dissolve via the flip-diffuse-detachment mechanism within the TLK framework (Fig. 4A). Notably, the width

of these ion clusters ranges from 0.5 to 0.6 nm, which aligns with the dimer width, measured at approximately 0.55 nm. These results imply that the Al dimers appear to be metastable on the surface without undergoing dissociation before detachment. However, the precise energy landscape governing the release of surface-diffusing dimers remains unclear. Furthermore, why one configurational arrangement of dimers dissolves preferentially over another is still not fully understood.

Anisotropic Detachment of Aluminates from the Acute and Obtuse Side. To interpret the experimental observations of the dissolution of armchair edges, we employed density functionalbased tight-binding (DFTB; see details in SI Appendix, Supplementary Text) molecular dynamics simulations with a gibbsite surface pit/solution model (Fig. 5 and SI Appendix, Figs. S17–S19), exploring the free energy landscape of aluminate dimer/monomer detachment from the armchair edges on the (002) plane. We separated the treatment of the monomer detachment and that of the dimer detachment by constraining the Al-Al distance during the dissolution of the dimer. Of course, the detachment coordinate (here the height) could be coupled to the separation of the dimer into monomers, but the two-dimensional mapping of the free energy landscape would be computationally intractable even at the DFTB level. The detachment of the Al dimer results in the presence of two five-coordinated Al sites, less thermodynamically stable than the six-coordinated sites (38, 39), yet change in coordination is a rare event. While ¹H-²⁷Al CP-MAS NMR could be envisioned for detecting such surface species [as it can be for materials like the allophane layer of aluminosilicates (46)], it would not be surface-selective for gibbsite due to its ubiquitous bulk hydroxyl groups, although direct polarization

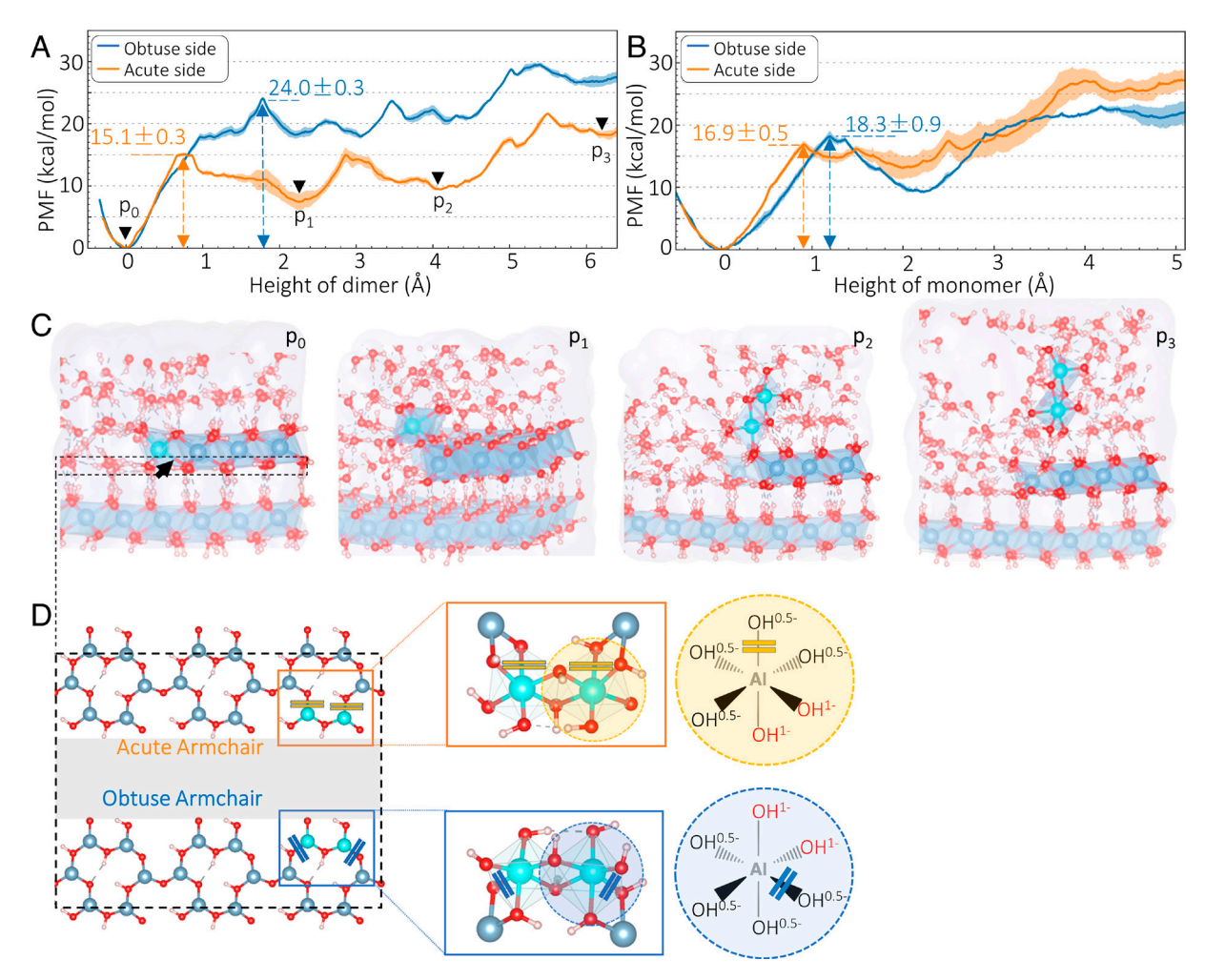


Fig. 5. DFTB simulation of the detachment of aluminate dimer and monomer from armchair step-edges on gibbsite (002) plane. (A) PMFs of an aluminate dimer detaching from opposite [010] and [$0\overline{1}$ 0] step edges; The shading in the plot indicates the SD; The initial state (p_0), metastable state after breaking the first two Al-OH-Al bridges (p_1) and the third bridge (p_2), and the final product completely detached (p_3) are shown by arrows. (B) PMFs of an aluminate monomer detaching from opposing [010] and [$0\overline{1}$ 0] step edges. (C) Snapshots of p_0 , p_1 , p_2 , and p_3 in molecular simulation of detachment of dimer. (D) The Al-OH-Al linkage network that faces the underlying gibbsite sheet shows the structure difference of first breaking linkage of opposing armchair step edges.

²⁷Al MAS NMR has identified trace amounts of penta-coordinate Al in dried gibbsite powder (47). Therefore, two hydroxide (OH-) anions present in the solution before the Al detachment are manually attached to the Al sites following the disruption of the initial two bridges. The potentials of mean force (PMF) for the detachment of an aluminate dimer from the opposite sides of [010] step edges (Fig. 5A) effectively distinguish the dimer detachment process on opposite sides of a surface trench. The results reveal an energy barrier of approximately 15.1 ± 0.3 kcal/ mol at the acute edge for the aluminate dimer to flip up (the first and largest one); this involves the simultaneous breaking of the bottom two Al-O bridges [Fig. 5C(p1)]. Conversely, at the obtuse side, the energy barrier for dimer flipping increases to around 24.0 ± 0.3 kcal/mol, with the first two bridge breakages occurring sequentially without a stable intermediate state. Rotating the unit cell allows for the construction of a trench with another armchair edge using the same approach, and the PMFs are calculated for this configuration as well. A similar trend is observed at $\begin{bmatrix} 3 \ \overline{1} \ 0 \end{bmatrix}$ edges, with the dimer detachment at the acute edge having a lower energy barrier compared to that at the obtuse side, consistent with the findings for the [0 1 0] trench (SI Appendix, Fig. S20).

To determine whether the anisotropic dissolution of armchairs occurs via a monomer-by-monomer mechanism, we simulated the

detachment of monomers from acute [0 1 0] and obtuse [0 1 0] armchair edges, examining corresponding PMFs. The results show consistent free energy profiles for the detachment of two monomers with close but higher energy barriers (16.9 ± 0.5 and 18.3 ± 0.9 kcal/mol) than that of the dimer detachment from the acute edge (Fig. 5B). Taking the ratio of monomer-to-dimer detachment rates to be given by $\exp(-\Delta F_d^*/RT)/\exp(-\Delta F_m^*/RT)$, where ΔF_d^* and $\Delta F_{m}^{\#}$ are the first, rate-limiting free energy barriers to acute edge dimer and acute edge monomer detachment, respectively, indicates that over 95% of the initial detachment event will be that of the dimer at acute. On the contrary, on the obtuse side the likely mechanism is the monomer detachment ($\Delta F^{\#}$ = 18.3 ± 0.9 kcal/mol) rather than the dimer detachment ($\Delta F^{\#}$ = 24.0 ± 0.3 kcal/mol). Therefore, the 3.2 kcal/mol difference in free energy barriers for dissolution between the acute and obtuse sides, as predicted by simulations, indicates that the dissolution rate of the acute side is two orders of magnitude faster than that of the obtuse side. This prediction closely aligns with the one-order-of-magnitude difference in apparent dissolution rates observed in AFM studies (SI Appendix, Fig. S8). Notably, the activation barriers estimated from PMF simulations (15 to 24 kcal/mol) fall within a realistic and experimentally reported range for gibbsite dissolution processes (11 to 32 kcal/mol) (17, 42, 48–50), supporting the physical relevance of the simulated detachment mechanisms. These results show the dimeric detachment from the acute armchair is the key to replicating the anisotropic dissolution of the gibbsite and kinetically supports the dimeric detachment mechanisms.

To gain chemical insight into dissolution anisotropy, we performed a detailed analysis of the edge structures, focusing on the breaking of the first two Al-O bonds that constitute the rate-limiting step, given that the bond-breaking rates at >Al-µ₂-OH-Al< bridges of MAl₁₂ Keggin-type polyoxometalate are highly sensitive to bonding details (3, 40). The six-coordinated edge Al atoms use their 3porbitals to bond with the first-coordinated O atoms. Notably, there are two general types of OH groups based on the formal charge analysis at the edges: bridge μ_2 -OH with a formal charge of -0.5, and dangling η -OH with a formal charge of -1 (Fig. 5*D*). For both acute and obtuse armchair edges, the first bridges to break during dimer detachment are the lower two Al-OH-Al bridges that face the underlying gibbsite sheet. At the acute edge, these Al-O bridge bonds are positioned *trans* to the edge's dangling OH groups (-1). In contrast, at the obtuse edge, the first two bonds to break are *trans* to the bridge OH groups (-0.5) between the two edge dimer Al atoms. On the acute side, the imbalance of the OH groups at the transposition of the edge Al site causes polarization in the Al p-orbital: more electron density is present on the OH (-1) side, indicating stronger bonding, while less overlap occurs at the OH (-0.5) side with the edge Al, signifying a weaker bond connecting the dimer to the edge. As a result, these bonds are more likely to break at the acute edges, leading to a lower energy barrier and, consequently, a faster dissolution rate. To complement this orbital description, we sampled the two lower bridge Al-O bond length distributions at both edges within a 100 ps molecular dynamics run [visualized using boxplots (SI Appendix, Fig. S21)]. The Al-O bonds at the acute edge are generally longer than those at the obtuse side which agrees with the "trans effect" hypothesis that the Al-O bonds trans to the dangling OH- are weakened (51, 52).

From the above findings, we conclude that the Al-dimer is the reactive unit for the dissolution of gibbsite in alkaline solution and is the complement to crystallization via attachment of polynuclear clusters reported for calcite (24). The general importance of anisotropic dissolution of Al-dioctahedral sheet for Al-octahedra-containing phyllosilicates, including muscovite (53), illite (54), and apophyllite (55), is clear from previous observations of a characteristic interlaced pattern connecting adjacent layers of dissolution spirals. Our results can help to rationalize the observations of anisotropic dissolution of a wide range of minerals containing Al octahedra (56, 57). On the other hand, our results may also provoke conceptual models of mineral dissolution/ growth via dimers or oligomers. The physical adsorption of solutes on mineral surfaces could create a local concentration of monomers high enough for dimers/oligomers to be thermodynamically stable (28, 58), where the dissolution/growth is kinetically favorable through detaching/attaching of polynucleate complexes (24).

In interfacial chemistry, characterization of metastable intermediates during dissolution, nucleation, and growth is the key to understanding reactive sites and fundamental dynamics. The results presented here demonstrate that HS-AFM can now be integrated temporally and spatially with theoretical simulations based on first principles and enhanced sampling methods, offering a paradigm for the study of fundamental interfacial reaction mechanisms.

Materials and Methods

Synthesis of Gibbsite Nanoplates. Gibbsite nanoplates were synthesized using a two-step method (33). Specifically, 0.25 M aluminum (Al) [Al(NO₃)₃·9H₂O, \geq 98%, Sigma-Aldrich] was dissolved in deionized water (18.20 M Ω /cm) with stirring, and the pH was adjusted to approximately 5.0 by adding a 3 M sodium hydroxide (NaOH) (≥98%, Sigma-Aldrich) aqueous solution. The resulting solution was continuously stirred for 1 h and then centrifuged to collect gel-like precipitates. The gel was washed three times with deionized water and dispersed into deionized water to create 0.25 M-Al suspensions. Subsequently, 16 mL of the gel solution was transferred into a 20 mLTeflon vessel, which was then sealed within a Parr bomb and heated at 80 °C for 5 d. Finally, the resulting white product was collected by centrifugation, washed three times with deionized water, and dried at 50 °C overnight.

Solids Characterization. XRD patterns were obtained utilizing a Philips X'pert Multi-Purpose Diffractometer (PANalytical, Almelo, The Netherlands) outfitted with a stationary Cu anode running at 50 kV and 40 mA. The XRD patterns were documented within a 10 to 70° 20 range. Phase identification was accomplished through the application of JADE 9.5.1 (Materials Data Inc.) and the 2012 PDF4+ database from the International Center for Diffraction Data. TEM samples were prepared by dispersing in deionized water through 5-min sonication and subsequently dropping the resulting mixture onto copper grids (Lacey Carbon, 300 mesh, Ted Pella, Inc.). The grids were then air-dried under ambient conditions. An aberration-corrected FEI Titan field emission TEM was employed to carry out the TEM analysis, with all samples being imaged at an acceleration voltage of 300 kV.

In Situ AFM. Before preparing the AFM samples, the gibbsite suspension was washed with ACS reagent pure water (LP366, Honeywell) three times by centrifuge to clear the possible dissolved free Al ions or other contaminations. The substrate TiO_2 (001) wafer was also cleaned by plasma for 5 min. TiO_2 was selected as a substrate because they are stable under the alkaline solution we use (59). Around 50 μ L, 20 mg/L gibbsite suspension was dropped on the TiO₂ (001) wafer. Then we blow-dried the wafer using compressed ultrapure (>99.99%) N₂ gas to clean the particles that were not physically adsorbed to the substrate, to avoid the particle drifting during AFM measurement. We used Cypher VRS AFM to perform all AFM measurements under a static solution at 20 °C within an air chamber to avoid the evaporation of the solution. More than 100 μL NaOH (≥98%, Sigma-Aldrich) agueous solution (LP366, Honeywell) was dropped on the wafers. Therefore, the total concentration of AI on the wafer is less than 0.13 mM, which makes sure the solution is far from saturation even if all particles are dissolved in 0.1 M NaOH. The FASTSCAN-B AFM tips (Bruker Inc.) with a spring constant of 1.8 N/m were utilized here. To evaluate the dissolution kinetics of gibbsite at various NaOH concentrations (0.01 to 0.4 M), the AFM tip was brought to the sample surface using the amplitude mode, and the scan rate for dissolution kinetics images was set to 2 Hz (128 s per image). The scan was conducted over 20 min, resulting in more than 10 images (256 × 256 pixels) to calculate the dissolution rate. Additionally, high-resolution images of gibbsite were obtained by scanning the AFM tip over a $20 \times 20 \text{ nm}^2$ area at a scan rate of 2 to 14 Hz (18 to 128 s per image). The AFM images were analyzed by using the software Gwyddion 2.63 (60) and the software ImageJ (61). The dissolution rates of the step edges at 0.4 NaOH are not measured because the retreat velocity is too fast to follow the single change of a single edge.

In Situ ²⁷Al NMR and Raman spectroscopy. In situ ²⁷Al NMR spectroscopy was used to characterize dissolving Al(OH)₄ ions from 1 g/L gibbsite in 0.2 M NaOH at 20 °C. First, a concentration calibration curve was prepared. Gibbsite (1 g/L) was dispersed in 0.2 M NaOH at 20 °C. After approximately 1 d, the sample was filtered. Samples were prepared via serial dilutions with 0.2 M NaOH solution. The concentrations of Al(OH) $_{4}^{-}$ in this serial dilution series were then determined with Inductively Coupled Plasma Optical Emission spectroscopy. Then ²⁷Al NMR spectroscopy was performed on the dilution series of varying concentrations of Al(OH)₄ ions in 0.2 M NaOH to validate the linearity of the integral to the concentration of Al(OH)₄. The samples were contained in fluorinated ethylene polymer coaxial inserts placed into 5 mm outer diameter NMR tubes. After acquiring NMR spectra for this dilution series of varying concentrations and validating linearity of concentration versus signal integral, in situ ²⁷Al NMR data were acquired by dispersing 1 g/L of gibbsite in 0.2 M NaOH, loading this dispersion into a fluorinated ethylene polymer coaxial insert, which was then placed into a 5 mm outer diameter NMR tube and then immediately placed into the NMR spectrometer.

For both the calibration series and the in situ NMR experiment, single pulse direct excitation ²⁷Al NMR spectra were acquired on an 11.74TNMR spectrometer equipped with a broadband probe. At 11.74 T, the Larmor frequency of ²⁷Al is 130.287 MHz. Spectra were acquired with an excitation pulse width of 13.75 μs equivalent to a $\pi/2$ pulse length, at an acquisition time of 200 ms enumerated with 5,209 complex points, a recycle delay of 250 ms, a sweep width of 26041.7 Hz, and with 16 transients for the in situ data leading a total acquisition time per data point of 8 s. For the calibration curve, the same parameters were used except that 128 transients were acquired for each concentration. Postacquisition processing was performed in Mestrenova (version 14.01-23559, released 2019-06-07, Mestrelab Research S.L.) where the spectra were zero-filled to 16,384 complex points and 5 Hz of exponential line broadening was applied. The baseline was corrected using a Whitaker smoother routine, and the integral of the signal was determined numerically.

Raman spectroscopy was used to monitor the phase change of solids during dissolutions. Raman spectra were acquired with a Horiba LabRam HR spectrometer installed on an inverted optical Nikon Ti=E microscope using a 632.8 nm HeNe laser light source.

Surface Structure Reconstruction from AFM Image Assisted by ML. A customized ML based tracking algorithm with a customized pretrained U-Net neural network was used to track the Al atom positions from AFM following our previous work (62). In typical image processing, the raw images (256 \times 256 pixels) were cropped into 128 \times 128-pixel blocks as input to the U-Net. A customized MATLAB code was used to perform an eight-times-up sampling to the prediction results and to identify the aluminum with a pattern-matching method.

One critical factor of neural network performance is the preparation of training datasets. To generate realistic AFM images with ground truth of Al atom positions, we developed a workflow to simulate AFM images based on atomic models of gibbsite (001) surface and Si tip. We used the CLAYFF force field (45) in the interaction calculation, and the zero planes of the z-direction force component then proceeded in the image simulation, to further add thermal noise and scan noise textures (detailed in *SI Appendix, Supplementary Text*). A few examples of simulated images are shown in *SI Appendix*, Fig. S15.

As the pixel size in our data is 0.78 Å, ~40% of Al-O bond length, predicting the

As the pixel size in our data is 0.78 Å, ~40% of Al-O bond length, predicting the Al position in pixel size level is not good enough. As an alternative to conventional binarization, we encoded the ground truth of the Al atom position as an image, with each Al atom as a 2-dimensional isotropic Gaussian peak with a sigma of 0.5 (*SI Appendix*, Fig. S16). Instead of conventional binarization of an image, we use the U-Net to predict continuous values and reconstruct the Al atom position with an eightfold up-sampling using the pattern convolution method. The small positional error on the validation dataset indicates that the model is well trained (*SI Appendix*, Fig. S16).

Development of the DFTB Model.

Parameterization. Building upon previous work for aluminate dimerization (63), our SCC-DFTB set for Al reactivity in aqueous conditions was refined. The training set now includes DFT and DLPNO-CCSD(T) reaction energies in implicit water solvation. The following transformations were considered in the fit.

Chemical reactions. Monomer dissociation from a zigzag edge cluster model (relaxed energy scan):

$$AI(OH)_4^- = AI(OH)_3 + OH^-,$$
 [1]

$$AI(OH)_4^- + H_2O = AI(OH)_3H_2O,$$
 [2]

$$AI(OH)_4^- + OH^- = AI(OH)_5,$$
 [3]

2
$$AI(OH)_4^- = AI_2(OH)_7^- + OH^-,$$
 [4]

2
$$AI(OH)_4^- = AI_2(OH)_6 + 2 OH^-,$$
 [5]

2
$$AI(OH)_4^- = AI_2O(OH)_6^{2-} + H_2O,$$
 [6]

2
$$AI(OH)_4^- = AI_2(OH)_8^{2-}$$
, [7]

3
$$AI(OH)_4^- = AI_3(OH)_9 + 3 OH^-,$$
 [8]

4
$$AI(OH)_{4}^{-} = AI_{4}(OH)_{12} + 4 OH^{-},$$
 [9]

Hydrogen bonding:

$$2 H_2 O = (H_2 O)_2,$$
 [10]

$$6 H_2 O = (H_2 O)_{6'}$$
 [11]

2
$$AI(OH)_4^- = (AI(OH)_4^-)_2$$
. [12]

All the geometries were obtained using M06-2X-D3/def2-TZVPPD and DFT electronic energies were obtained at the DLPNO-CCSD(T)/aug-cc-pVTZ level except for the monomer dissociation that was obtained using M06-2X-D3/def2-TZVPPD. All DFT calculations were done using the SMD solvation model (64) for water and employed the ORCA code (65). The following procedure was employed for DFTB parameterization:

- (i) A first fit was performed to obtain the integral tables for each element-element pair. Using the Hotbit code (66), radii of the harmonic potentials used to confine the pseudo-atomic orbitals were fitted based on a subset of the training set. Repulsive potentials of all the pairs except Al-O and O-H were generated using the same code.
- (ii) For a series of fixed values of $\gamma_{\alpha,H}$ [the damping term for X-H pairs (67)], Hubbard parameters and parameters of the Al-O and O-H repulsive potentials of the form $\exp{(-a_1r+a_2)}$ were fitted by minimizing the atomic forces of the DFT-optimized molecules and the error in reaction electronic energies. The $\gamma_{\alpha,H}$ value leading to the correct liquid water density and to the gibbsite lattice parameters the closest to the experiment was retained. The fit was performed using an in-house script and employed a Nelder-Mead minimizer (68). DFTB calculations employed the SMD solvation model and were performed using GAMESS-US (69).

Finally, to make it continuous at the upper cutoff for molecular dynamics, the repulsive potential was augmented by piecewise polynomial splines.

Validation. After parameterization of the DFTB model, umbrella sampling (US) was performed using the Al-Al coordination number (CN(Al-Al)) as the biased collective variable (CV) to sample the start of the dissociation of a monomer from a zigzag step edge and armchair step edge in pure water using starting structures from previous work (39). CN(Al-Al) was restrained to values ranging from 4.0 to 5.0 by increments of 0.1 using a force constant of 500 kcal/mol/ \mathring{A}^2 . The same procedure was performed using ab initio molecular dynamics with the RPBE-D3 (70, 71) functional and the TZVP-MOLOPT-SR-GTH (72) basis set. Both sets of simulations were performed in CP2K (73) and PLUMED (74) was used to apply the harmonic restraints. SI Appendix, Fig. S17 shows that after shifting the DFTB potential of mean force along CN(Al-Al), the change in free energy is almost identical to the DFT one. The different location of the minima is simply due to slightly different positions of one gibbsite layer with respect to the other one, since the switching function for $CN(AI-AI)[1-(r/r_0)]$ NN)/ $(1 - (r/r_0)MM)$] with r0 = 4.0 Å, NN = 9, and MM = 14, includes secondneighbor contributions.

To assess the ability of the DFTB model to capture trends in gibbsite detachment energies, we performed a series of static calculations using both DFT and DFTB to evaluate the dissociation of aluminum units from four distinct sites on a cluster model of the gibbsite sheet, incorporating SMD implicit solvation. Using the r²SCAN-3c DFT functional (75), the distances between the dissociating Al and two other Al atoms were constrained and scanned over a range encompassing the nondissociated state and the first dissociation barrier. The geometry was relaxed at every step. Electronic energies were then computed using DFTB and four different DFT functionals with the ma-def2-TZVPP basis set: r²SCAN-3c(meta-GGA), M06-2X-D3 (hybrid meta-GGA) (71, 76), ωB97M-D4 (range-separated hybrid meta-GGA) (77), and revDSD-PBEP86-D4 (spin-component-scaled double-hybrid GGA) (78). The respective WTMAD-2 errors for the general chemistry GMTKN55 benchmark database (79) are 7.5 (75), 5.0 (79), 4.1 (77), and 2.1 (78) kcal/mol, respectively. The energy profiles for the four sites and the corresponding energy barriers are shown in SI Appendix, Fig. S18. The mean absolute deviations of the barriers relative to revDSD-PBEP86-D4 are 4.1, 1.5, 4.2, 0.3 kcal/mol for DFTB, r²SCAN-3c, M06-2X-D3, and $\omega B97M\text{-}D4$, respectively. These results indicate that the DFTB model achieves a barrier prediction accuracy comparable to that of M06-2X-D3, a widely used and reliable hybrid functional (79). This comparison supports the reliability of our DFTB model in predicting free energy barriers for Al unit dissociation from gibbsite step edges under aqueous conditions.

US Simulations of Dissolution Based on the DFTB Model. We introduce DFTB simulations utilizing a gibbsite surface pit/solution model. These simulations are aimed at exploring the dissolution kinetics of aluminate dimer and monomer detachment occurring at the armchair edges: [010] and [3-10] on the (002) plane.

The surface consists of two gibbsite layers, with the bottom layer representing the complete gibbsite bulk. To mimic the step-edges structure observed in AFM images, several columns of Al(OH)₃ units were selectively removed along specific directions ([010] or [310]), creating a trench. This approach is consistent with our previous work (39). For the investigation of dimer detachment, only the armchair edges are considered. The aluminum atoms at these edges are saturated by OH⁻ groups, representing a high pH condition (80). Then a slab of water is added into the system and an NPT run is carried out for more than 8 ps till the volume becomes stable, additional more than 10 ps NVT simulation is performed to pre-equilibrate the system before the US simulations. The detachment of the Al dimer results in the presence of two five-coordinated Al sites, less thermodynamically stable than the six-coordinated sites (30, 32), yet change in coordination is a rare event. Therefore, two hydroxide (OH-) anions present in the solution before the Al detachment are manually attached to the Al sites following the disruption of the initial two bridges. The overall charge of the system is -10, with eight OH ions bonded to the edge aluminum sites and two OH⁻ ions present in the solution. Considering the thick water layer (>10 Å), coulombic effect would be greatly reduced by the water molecules' orientation rearrangement and will barely affect the dimer/monomer detachment process. For the cases of monomer detachment, one additional OH⁻ anion is introduced to the solution to restore the edge aluminum sites after monomer detachment. The simulation box dimensions are 17.48 $\textrm{Å} \times 20.45 \, \textrm{Å} \times$ 19.25 Å, which includes over 10 Å of water in the bulk region after undergoing pre-equilibration through NPT ensemble simulations.

- A. Putnis, Why mineral interfaces matter. Science 343, 1441-1442 (2014).
- C. Fischer, I. Kurganskaya, T. Schäfer, A. Lüttge, Variability of crystal surface reactivity: What do we know? Appl. Geochem. 43, 132-157 (2014).
- C. A. Ohlin, E. M. Villa, J. R. Rustad, W. H. Casey, Dissolution of insulating oxide materials at the molecular scale. Nat. Mater. 9, 11-19 (2010).
- A. C. Lasaga, A. Luttge, Variation of crystal dissolution rate based on a dissolution stepwave model. Science 291, 2400-2404 (2001).
- W. H. Casey, C. Ludwig, The mechanism of dissolution of oxide minerals. Nature 381, 506-509 (1996)
- K. Miyata et al., Dissolution processes at step edges of calcite in water investigated by high-speed frequency modulation atomic force microscopy and simulation. Nano Lett. 17, 4083–4089 (2017).
- P. G. Vekilov, What determines the rate of growth of crystals from solution? Crystal Growth Design 7,
- I. Kurganskaya, A. Luttge, A comprehensive stochastic model of phyllosilicate dissolution: Structure and kinematics of etch pits formed on muscovite basal face. Geochim. Cosmochim. Acta 120, 545-560 (2013).
- I. Kurganskaya, A. Luttge, Kinetic monte carlo simulations of silicate dissolution: Model complexity and parametrization. J. Phys. Chem. C 117, 24894-24906 (2013).
- 10. I. Kurganskaya, S. V. Churakov, Carbonate dissolution mechanisms in the presence of electrolytes revealed by grand canonical and kinetic Monte Carlo modeling. J. Phys. Chem. C 122, 29285-29297 (2018).
- T. F. Bates, "Halloysite and gibbsite formation in Hawaii11Contribution no. 60-51, Mineral Industries Experiment Station, The Pennsylvania State University, University Park, Pennsylvania" in Clays and Clay Minerals, E. Ingerson, Ed. (Pergamon, 1962), pp. 315-328, 10.1016/B978-1-4831-9842-2.50022-5.
- T. G. Pearson, The Chemical Background of the Aluminium Industry (Royal Institute of Chemistry,
- S. Goldberg, J. A. Davis, J. D. Hem, "The surface chemistry of aluminum oxides and hydroxides" in The Environmental Chemistry of Aluminum, G. Sposito, Ed. (CRC Press, Boca Raton, FL, ed. 2, (2020),
- Y. Lucas, F. J. Luizao, A. Chauvel, J. Rouiller, D. Nahon, The relation between biological activity of the rain forest and mineral composition of soils. Science 260, 521-523 (1993).
- R. A. Peterson et al., Review of the scientific understanding of radioactive waste at the U.S. DOE hanford site. Environ. Sci. Technol. 52, 381-396 (2018).
- T. Boschetti, L. Toscani, Springs and streams of the Taro-Ceno Valleys (Northern Apennine, Italy): Reaction path modeling of waters interacting with serpentinized ultramafic rocks. Chem. Geol. 257, 76-91 (2008).
- J. Addai-Mensah, J. Dawe, J. Ralston, "The dissolution and interactions of gibbsite particles in alkaline media" in Developments in Mineral Processing, P. Massacci, Ed. (Elsevier, 2000), vol. 13, pp
- A. C. Lasaga, A. LÜTTGE, A model for crystal dissolution. Eur. J. Mineral. 15, 603-615 (2003).
- P. M. Dove, N. Han, J. J. De Yoreo, Mechanisms of classical crystal growth theory explain quartz and silicate dissolution behavior. Proc. Natl. Acad. Sci. U.S.A. 102, 15357-15362 (2005).
- M. Zhu et al., In situ structural characterization of ferric iron dimers in aqueous solutions: Identification of μ -oxo species. *Inorg. Chem.* **52**, 6788-6797 (2013).

In our study, we employ the relative height between the center of mass of the studied Al atom(s) and the remaining Al atoms in the gibbsite slab as the CV for conducting US simulations. All the simulations are performed with CP2K code (73). Proper harmonic restraints through the PLUMED interface are applied to ensure the proper restraint of the CV within each window as well as sufficient sampling overlap among the windows (74). Each window involves NVT simulations exceeding 46 ps, employing the Nosé-Hoover thermostat (81, 82). The simulations are performed with a time step of 0.5 fs, and the final 18 ps of the trajectories are utilized to reconstruct the PMFs. The 18 ps trajectories are split into three 6 ps blocks to confirm the convergency of PMFs and to calculate the error bars as shown in the PMFs plots. The PMF reconstruction is achieved using Grossfield's weighted histogram analysis method code (83).

Data, Materials, and Software Availability. All study data are included in the article and/or supporting information. The Jupyter Notebook Python script of a U-Net training example can be found on GitHub: https://uofi.box.com/s/ k45wffrq3xf04taa7yeir19cqijyt7of (84).

ACKNOWLEDGMENTS. We thank Prof. William H. Casey for the fruitful discussion and Dr. Shuai Zhang for his help in AFM data analyses. This research was supported by Ion Dynamics in Radioactive Environments and Materials, an Energy Frontier Research Center funded by the U.S. Department of Energy (DOE), Office of Science, Basic Energy Sciences under FWP 68932. A portion of the work was carried out in the Environmental and Molecular Sciences Laboratory, a national scientific user facility at Pacific Northwest National Laboratory (PNNL) sponsored by the DOE's Office of Biological and Environmental Research, under user proposals 61223 (10.46936/lsr. proj.2024.61223/60012698), 51382 (10.46936/lser.proj.2020.51382/60000186), and 51922 (10.46936/lser.proj.2021.51922/60000373). PNNL is a multi-program national laboratory operated by Battelle Memorial Institute under contract no. DE-AC05-76RL01830 for the DOE.

- 21. M. Zhu et al., Precipitation pathways for ferrihydrite formation in acidic solutions. Geochim. Cosmochim. Acta 172, 247–264 (2016).
- T. R. Graham et al., Intermediate species in the crystallization of Sodium Aluminate Hydroxy Hydrates. J. Phys. Chem. C 124, 12337-12345 (2020).
- A. S. Zadeh, B. G. Peters, On dimerization kinetics and boundary layer transport in crystal growth from dimers. J. Cryst. Growth 601, 126913 (2023).
- M. P. Andersson et al., A microkinetic model of calcite step growth. Angew. Chem. Int. Ed. Engl. 55, 11086-11090 (2016).
- O. Sadeghi, L. N. Zakharov, M. Nyman, Aqueous formation and manipulation of the iron-oxo Keggin ion. Science 347, 1359-1362 (2015).
- J. S. Weatherill et al., Ferrihydrite formation: The role of Fe13 Keggin clusters. Environ. Sci. Technol. 50, 9333-9342 (2016).
- R. L. Penn, J. F. Banfield, Oriented attachment and growth, twinning, polytypism, and formation of metastable phases: Insights from nanocrystalline TiO2. Am. Mineral. 83, 1077-1082 (1998).
- G. Zhu et al., Self-similar mesocrystals form via interface-driven nucleation and assembly. Nature **590**, 416-422 (2021).
- D. Li et al., Direction-specific interactions control crystal growth by oriented attachment. Science **336**, 1014-1018 (2012).
- P.-A. Fang, J. F. Conway, H. C. Margolis, J. P. Simmer, E. Beniash, Hierarchical self-assembly of amelogenin and the regulation of biomineralization at the nanoscale. Proc. Natl. Acad. Sci. U.S.A. 108, 14097-14102 (2011).
- M. P. Boneschanscher et al., Long-range orientation and atomic attachment of nanocrystals in 2D honeycomb superlattices. Science 344, 1377-1380 (2014).
- G. Zhu et al., Crystal dissolution by particle detachment. Nat. Commun. 14, 6300 (2023).
- S. Wang et al., Two-step route to size and shape controlled gibbsite nanoplates and the crystal growth mechanism. Crystengcomm 22, 2555-2565 (2020).
- X. Zhang et al., Fast synthesis of gibbsite nanoplates and process optimization using box-behnken experimental design. Crystal Growth Design 17, 6801-6808 (2017).
- H. Saalfeld, M. Wedde, Refinement of the crystal structure of gibbsite, A1(OH)3. Zeitschrift für Kristallographie 139, 129-135 (1974).
- C. D. Peskleway, G. S. Henderson, F. J. Wicks, Dissolution of gibbsite: Direct observations using fluid cell atomic force microscopy. Am. Mineral. 88, 18-26 (2003).
- S. J. Freij, G. M. Parkinson, Surface morphology and crystal growth mechanism of gibbsite in industrial Bayer liquors. Hydrometallurgy 78, 246–255 (2005).
- X. Liu, J. Cheng, M. Sprik, X. Lu, R. Wang, Understanding surface acidity of gibbsite with first principles molecular dynamics simulations. Geochim. Čosmochim. Acta 120, 487-495 (2013).
- Q. Guo, M. Pouvreau, K. M. Rosso, A. E. Clark, Mechanisms of dissolution from Gibbsite step edges elucidated by ab initio molecular dynamics with enhanced sampling. Geochim. Cosmochim. Acta 366, 201-209 (2024).
- J. R. Rustad, J. S. Loring, W. H. Casey, Oxygen-exchange pathways in aluminum polyoxocations1 1Associate editor: D. Geochim. Cosmochim. Acta 68, 3011-3017 (2004).
- C. Ludwig, W. H. Casey, On the mechanisms of dissolution of bunsenite [NiO(s)] and other simple oxide minerals. J. Colloid Interface Sci. 178, 176-185 (1996).
- L. Bao et al., The most probable mechanism function and kinetic parameters of gibbsite dissolution in NaOH. Chin. J. Chem. Eng. 18, 630-634 (2010).

- E. T. Nienhuis et al., Structure and reactivity of sodium aluminate complexes in alkaline solutions. J. Mol. Liq. 367, 120379 (2022).
- M. Pouvreau et al., Ab initio molecular dynamics reveal spectroscopic siblings and ion pairing as new challenges for elucidating prenucleation aluminum speciation. J. Phys. Chem. B 122, 7394–7407 (2018)
- R.T. Cygan, J.-J. Liang, A. G. Kalinichev, Molecular models of hydroxide, oxyhydroxide, and clay phases and the development of a general force field. J. Phys. Chem. B 108, 1255–1266 (2004).
- C. W. Childs, S. Hayashi, R. H. Newman, Five-coordinate aluminum in allophane. Clays Clay Miner. 47, 64-69 (1999).
- J. Z. Hu et al., Transitions in Al coordination during gibbsite crystallization using high-field 27Al and 23Na MAS NMR spectroscopy. J. Phys. Chem. C. 121, 27555-27562 (2017).
- J. A. M. Pereira et al., The kinetics of gibbsite dissolution in NaOH. Hydrometallurgy 96, 6–13 (2009).
- E.-S. A. Abdel-Aal, "Leaching kinetics of gibbsitic bauxite with sodium hydroxide" in Proceedings of the Mineral Engineering Conference (MEC 2016), P. B. Kowalczuk, J. Drzymała, Eds. (EDP Sciences, Les Ulis, France, 2016), p. 01021.
- R. Scotford, J. Glastonbury, Effect of temperature on the rates of dissolution of gibbsite and boehmite. Can. J. Chem. Eng. 49, 611–616 (1971).
- B. J. Coe, S. J. Glenwright, Trans-effects in octahedral transition metal complexes. Coord. Chem. Rev. 203, 5-80 (2000).
- 52. F. Basolo, R. G. Pearson, The trans effect in metal complexes. *Prog. Inorg. Chem.* **4**, 381–453
- K. J. Cantrell et al., "Characterization of solids in residual wastes from single-shell tanks at the hanford site Washington, USA-9277" in WM2009 Waste Management for the Nuclear Renaissance (WM Symposia Inc., Phoenix, Tempe, Arizona, 2009).
- (WM Symposia Inc., Phoenix, Tempe, Arizona, 2009).
 54. Y. Kuwahara, S. Uehara, Y. Aoki, Atomic force microscopy study of hydrothermal illite in Izumiyama pottery stone from Arita, Saga prefecture. Japan. Clays Clay Miner. 49, 300–309 (2001).
- K. Aldushin, G. Jordan, W. W. Schmahl, Kinematics of apophyllite leaching—A terrace-ledge-kink process within phyllosilicate interlayers. J. Cryst. Growth 297, 161–168 (2006).
- M.-P. Turpault, L. Trotignon, The dissolution of biotite single crystals in dilute HNO3 at 24 C: Evidence of an anisotropic corrosion process of micas in acidic solutions. *Geochim. Cosmochim. Acta* 58, 2761–2775 (1994).
- I. Kurganskaya, R. S. Arvidson, C. Fischer, A. Luttge, Does the stepwave model predict mica dissolution kinetics? Geochim. Cosmochim. Acta 97, 120–130 (2012).
- N. Deng et al., Organic-mineral interfacial chemistry drives heterogeneous nucleation of Sr-rich (Ba_{xr} Sr_{1,x})SO₄ from undersaturated solution. Proc. Natl. Acad. Sci. U.S.A. 116, 13221–13226 (2019).
- J. Schmidt, W. Vogelsberger, Aqueous long-term solubility of titania nanoparticles and titanium(IV) hydrolysis in a sodium chloride system studied by adsorptive stripping voltammetry. J. Solution Chem. 38, 1267–1282 (2009).
- D. Nečas, P. Klapetek, Gwyddion: An open-source software for SPM data analysis. Open Phys. 10, 181–188 (2012).
- T. J. Collins, ImageJ for microscopy. BioTechniques 43, S25–S30 (2007).
- L. Yao, Z. Ou, B. Luo, C. Xu, Q. Chen, Machine learning to reveal nanoparticle dynamics from liquidphase TEM videos. ACS Cent. Sci. 6, 1421–1430 (2020).
- M. Pouvreau et al., Mechanisms of Al3+ dimerization in alkaline solutions. Inorg. Chem. 59, 18181–18189 (2020).

- A. V. Marenich, C. J. Cramer, D. G. Truhlar, Universal solvation model based on solute electron density and on a continuum model of the solvent defined by the bulk dielectric constant and atomic surface tensions. J. Phys. Chem. B 113, 6378-6396 (2009).
- F. Neese, Software update: The ORCA program system-version 5.0. WIREs Comput. Mol. Sci. 12, e1606 (2022).
- P. Koskinen, V. Mäkinen, Density-functional tight-binding for beginners. Comput. Mater. Sci. 47, 237–253 (2009).
- P. Virtanen et al., SciPy 1.0: Fundamental algorithms for scientific computing in Python. Nat. Methods 17, 261–272 (2020).
- Y. Yang, H. Yu, D. York, Q. Cui, M. Elstner, Extension of the self-consistent-charge density-functional tight-binding method: Third-order expansion of the density functional theory total energy and introduction of a modified effective Coulomb interaction. J. Phys. Chem. A. 111, 10861–10873 (2007).
- M. W. Schmidt et al., General atomic and molecular electronic structure system. J. Comput. Chem. 14, 1347–1363 (1993).
- B. Hammer, L. B. Hansen, J. K. Nørskov, Improved adsorption energetics within density-functional theory using revised Perdew-Burke-Ernzerhof functionals. *Phys. Rev. B* 59, 7413–7421 (1999).
- S. Grimme, J. Antony, S. Ehrlich, H. Krieg, A consistent and accurate ab initio parametrization of density functional dispersion correction (DFT-D) for the 94 elements H-Pu. J. Chem. Phys. 132, 154104 (2010)
- J. Vande Vondele, J. Hutter, Gaussian basis sets for accurate calculations on molecular systems in gas and condensed phases. J. Chem. Phys. 127, 114105 (2007).
- J. Hutter, M. Iannuzzi, F. Schiffmann, J. VandeVondele, cp2k: Atomistic simulations of condensed matter systems. WIREs Comput. Mol. Sci. 4, 15-25 (2014).
- G. A. Tribello, M. Bonomi, D. Branduardi, C. Camilloni, G. Bussi, PLUMED 2: New feathers for an old bird. Comput. Phys. Commun. 185, 604–613 (2014).
- S. Grimme, A. Hansen, S. Ehlert, J.-M. Mewes, r2SCAN-3c: A "Swiss army knife" composite electronic-structure method. J. Chem. Phys. 154, 064103 (2021).
- Y. Zhao, D. G. Truhlar, The M06 suite of density functionals for main group thermochemistry, thermochemical kinetics, noncovalent interactions, excited states, and transition elements: Two new functionals and systematic testing of four M06-class functionals and 12 other functionals. *Theor. Chem. Acc.* 120, 215–241 (2008).
- A. Najibi, L. Goerigk, DFT-D4 counterparts of leading meta-generalized-gradient approximation and hybrid density functionals for energetics and geometries. J. Comput. Chem. 41, 2562-2572 (2020).
- G. Santra, M. Cho, J. M. L. Martin, Exploring avenues beyond revised DSD functionals: I. Range separation, with xDSD as a special case. J. Phys. Chem. A. 125, 4614-4627 (2021).
- L. Goerigk et al., A look at the density functional theory zoo with the advanced GMTKN55 database for general main group thermochemistry, kinetics and noncovalent interactions. Phys. Chem. Chem. Phys. 19, 32184–32215 (2017).
- Z. Śhen, S. N. Kerisit, A. G. Stack, K. M. Rosso, Free-energy landscape of the dissolution of Gibbsite at high pH. J. Phys. Chem. Lett. 9, 1809–1814 (2018).
- 81. D. J. Evans, B. L. Holian, The nose-hoover thermostat. *J. Chem. Phys.* **83**, 4069–4074 (1985).
- W. G. Hoover, Canonical dynamics: Equilibrium phase-space distributions. Phys. Rev. A 31, 1695 (1985).
- A. Grossfield, WHAM: The weighted histogram analysis method (2012). http://membrane.urmc. rochester.edu/content/wham. Accessed 5 April 2023.
- C. Qian, AFM image simulation. University of Illinois Box. https://uofi.app.box.com/s/ k45wffrq3xf04taa7yeir19cqijyt7of. Deposited 15 March 2024.